

Employing interfaces with metavalently bonded materials for phonon scattering and control of the thermal conductivity in TAGSx thermoelectric materials

Original

Employing interfaces with metavalently bonded materials for phonon scattering and control of the thermal conductivity in TAGSx thermoelectric materials / Rodenkirchen, C., Cagnoni, M., Jakobs, S., Cheng, Y., Keutgen, J., Yu, Y., Wuttig, M., Cojocarumiréidin, O.. - In: ADVANCED FUNCTIONAL MATERIALS. - ISSN 1616-3028. - STAMPA. - 30:17(2020), p. 1910039. [10.1002/adfm.201910039]

Availability:

This version is available at: 11583/2976033 since: 2023-02-14T13:46:18Z

Publisher:

Wiley

Published

DOI:10.1002/adfm.201910039

Terms of use:

This article is made available under terms and conditions as specified in the corresponding bibliographic description in the repository

Publisher copyright

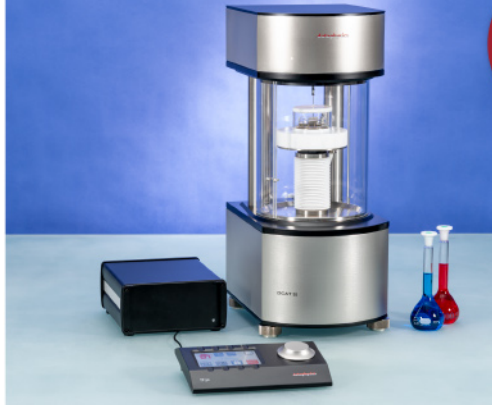
(Article begins on next page)



ASTM D5946
ASTM D7334
ASTM D7490
ISO 27448

optical contact angle measurements and drop contour analysis to determine surface energy as well as interfacial and surface tension

force tensiometry, dynamic contact angle measurements, and force of adhesion evaluation



ASTM D1331
ASTM D1417
ISO 1409

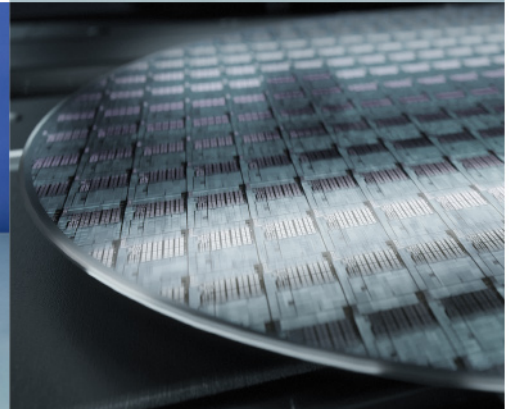


ISO/TR 13097

optical turbidity, stability and aging analysis of multi-phase dispersions



zeta potential measurements of fibres, powders, and plate-shaped solids



High-end, versatile laboratory measurement device portfolio for a comprehensive analysis of surfaces and interfaces

Learn more >

dataphysics
Understanding Interfaces

DataPhysics Instruments GmbH
Raiffeisenstraße 34 • 70794 Filderstadt, Germany
phone +49 (0)711 770556-0 • fax +49 (0)711 770556-99
sales@dataphysics-instruments.com
www.dataphysics-instruments.com

Employing Interfaces with Metavalently Bonded Materials for Phonon Scattering and Control of the Thermal Conductivity in TAGS-*x* Thermoelectric Materials

Cynthia Rodenkirchen, Matteo Cagnoni, Stefan Jakobs, Yudong Cheng, Jens Keutgen, Yuan Yu,* Matthias Wuttig, and Oana Cojocaru-Mirédin*

The thermoelectric compound $(\text{GeTe})_x(\text{AgSbTe}_2)_{1-x}$ in short (TAGS-*x*), is investigated with a focus on two stoichiometries, i.e., TAGS-50 and TAGS-85. TAGS-85 is currently one of the most studied thermoelectric materials with great potential for thermoelectric applications. Yet, surprisingly, the lowest thermal conductivity is measured for TAGS-50, instead of TAGS-85. To explain this unexpected observation, atom probe tomography (APT) measurements are conducted on both samples, revealing clusters of various compositions and sizes. The most important role is attributed to Ag_2Te nanoprecipitates (NPs) found in TAGS-50. In contrast to the Ag_2Te NPs, the matrix reveals an unconventional bond breaking mechanism. More specifically, a high probability of multiple events (PME) of $\approx 60\%$ is observed for the matrix by APT. Surprisingly, the PME value decreases abruptly to $\approx 20\text{--}30\%$ for the Ag_2Te NPs. These differences can be attributed to differences in chemical bonding. The precipitates' PME value is indicative of normal bonding, i.e., covalent bonding with normal optical modes, while materials with this unconventional bond breaking found in the matrix are characterized by metavalent bonding. This implies that the interface between the metavalently bonded matrix and covalently bonded Ag_2Te NP is partly responsible for the reduced thermal conductivity in TAGS-50.


1. Introduction

Thermoelectric devices convert heat into electricity and vice versa, being promising candidates for environmentally friendly

C. Rodenkirchen, Dr. M. Cagnoni, Dr. S. Jakobs, Y. Cheng, J. Keutgen, Dr. Y. Yu, Prof. M. Wuttig, Dr. O. Cojocaru-Mirédin
RWTH Aachen

I. Physikalisches Institut IA
Sommerfeldstraße 14, 52074 Aachen, Germany
E-mail: yu@physik.rwth-aachen.de;
cojocaru-miredin@physik.rwth-aachen.de

Prof. M. Wuttig
JARA-Institut Green IT
JARA-FIT
Forschungszentrum Jülich GmbH and RWTH Aachen University
52056 Aachen, Germany

 The ORCID identification number(s) for the author(s) of this article can be found under <https://doi.org/10.1002/adfm.201910039>.

© 2020 The Authors. Published by WILEY-VCH Verlag GmbH & Co. KGaA, Weinheim. This is an open access article under the terms of the Creative Commons Attribution License, which permits use, distribution and reproduction in any medium, provided the original work is properly cited.

DOI: 10.1002/adfm.201910039

power generation and refrigeration. The energy conversion efficiency is governed by the figure of merit of the material, expressed as $zT = S^2 \sigma T / \kappa$, where S is the Seebeck coefficient, σ is the electrical conductivity, κ is the total thermal conductivity, and T is the absolute temperature.^[1] Efficiencies above 30% can make thermoelectric devices highly attractive for future energy strategies. To this end, values of zT larger than 3 are required.^[2] Unfortunately, the interplay of several conflicting optimization parameters makes the design of thermoelectric materials very challenging. The “electron-crystal phonon-glass” concept enables a simplification of the problem.^[3] The thermal conductivity κ can be separated into an electronic component κ_e and a lattice component κ_l . Charge and lattice transport can be independently optimized to maximize $S^2 \sigma / \kappa_e$ and to minimize κ_l . A good thermoelectric material should hence carry electrons like a crystal and phonons like a glass.

Useful design strategies to increase the electrical transport properties include elemental doping to tailor the charge carrier concentration^[1] and to modify the band structure.^[4] For minimizing κ_l , however, a multitude of approaches has been adopted. Heavy atoms and soft bonds lead to slow phonon group velocity, while large unit cells and a high Grüneisen parameter enhance phonon Umklapp scattering.^[5] The total Grüneisen parameter γ_{tot} ($\gamma_{\text{tot}} = -\frac{\partial(\ln \omega)}{\partial(\ln V)} = -\frac{V}{\omega} \cdot \frac{\partial \omega}{\partial V}$, where V is the volume and ω is the frequency) is an average of the acoustic (γ_{ac}) and optical (γ_{opt}) parts, where the values of γ_{opt} are typically between 1 and 2 in most solids. Yet, many chalcogenides exhibit a significantly larger transverse optical Grüneisen parameter γ_{TO} , which has been associated with lone pairs first^[6] and subsequently with metavalent bonding (MVB).^[7,8] Further scattering channels for the phonons can be added by introducing lattice defects such as point defects, dislocations, and interfaces generated by grain boundaries or precipitates.^[5,9–11]

In this work, we are focusing on the impact of phase boundaries induced by nanoprecipitation on the thermal transport of compound $(\text{GeTe})_x(\text{AgSbTe}_2)_{1-x}$, commonly known by the acronym TAGS-*x* (*x* is the atomic percentage of GeTe). This

compound is one of the most studied chalcogenide systems for thermoelectric applications^[2] and has already been used in radioisotope generators in deep space missions.^[12,13] Many studies have been devoted to the goal of decreasing its lattice thermal conductivity κ_l by varying the composition. Two typical compounds, i.e., TAGS-80 and TAGS-85 have been reported as having the optimal thermoelectric properties.^[14–16] The low lattice thermal conductivity has been mainly related to the nanostructures such as precipitates.^[17] The size, structure, and composition of these precipitates are very often investigated using transmission electron microscopy (TEM), X-ray diffraction (XRD), and energy dispersive X-ray spectrometry (EDX).^[15,18,19] Yet, except for TEM, these methods possess a limited resolution and do not allow the investigation of very small precipitates (few nanometers) or metastable nuclei which are not accounted for by the phase diagram. Therefore, the purpose of the present work is to investigate the effect of nanoprecipitates (NPs) on the thermal conductivity κ of TAGS- x with various stoichiometries. This is accomplished by a combination of 3-omega and atom probe tomography (APT) measurements. The former enables the determination of the thermal conductivity, while the latter enables the determination of the composition of the material under study. APT is indeed a remarkable method for 3D atomistic distribution analysis that determines the composition at the nanoscale and allows for the identification of NPs.^[20,21] Hence, the present work enables a better understanding of the nature of the NPs in TAGS- x thin-film thermoelectric chalcogenides, which further confirms the role of nanostructures for the thermoelectric performance. Thin-film thermoelectrics are indeed very relevant for cooling application^[22] and for power generation.^[23] Moreover, this work proves for the first time the difference in bond breaking behavior at the nanoscale between the TAGS- x matrix and the existing Ag_2Te NPs.

Finally, the impact of matrix/ Ag_2Te interface on the phonon transport will be discussed from a chemical bonding perspective. Contrary to the covalently bonded Ag_2Te precipitates, the TAGS matrix is metavalently bonded. The work by Lee et al.^[7] has discussed the lattice thermal conductivity of metavalently bonded materials.^[24,25] Materials with MVB show inherently a low thermal conductivity^[8,24] because of the pronounced anharmonicity of the bonds and the small bond stiffness, which in turn leads to a large Grüneisen parameter and low phonon group velocity, respectively, both resulting in a low thermal conductivity.

2. Results and Discussions

TAGS- x with x equals to 15, 30, 50, 60, 70, and 85 have been investigated by XRD. All samples investigated can be fitted by assuming a rhombohedrally distorted rock-salt structure. AgSbTe_2 -rich samples (TAGS-15 and TAGS-40) exhibit some small additional peaks which can be explained by a secondary rock-salt crystal structure (Fm-3m). These additional peaks are negligibly small in TAGS-50 and TAGS-70 and are not found in TAGS-85.

In the present study, we focus on the samples TAGS-85 and TAGS-50. Their corresponding XRD pattern can be seen in Figure 1. TAGS-85 was chosen because of its importance as a

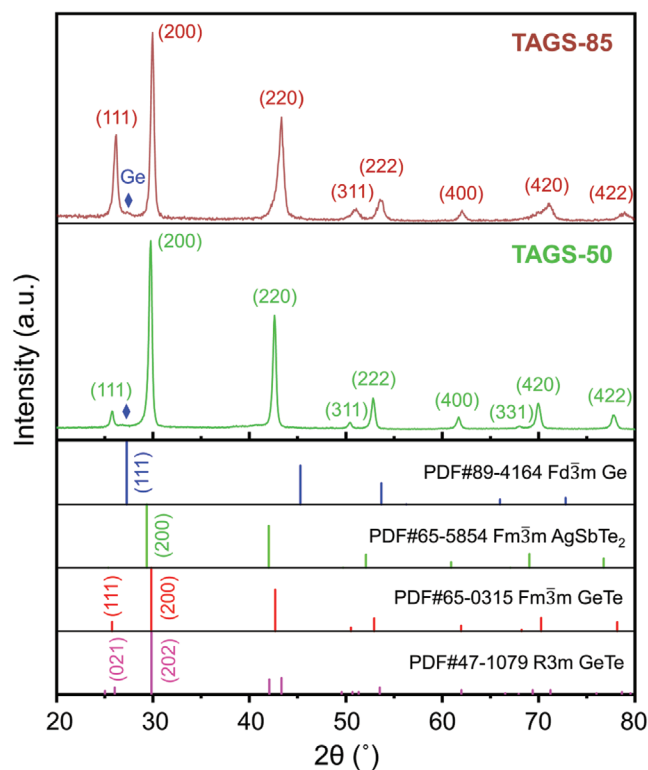


Figure 1. XRD pattern of TAGS-50 and TAGS-85.

thermoelectric material, while TAGS-50 serves as a counterpart to TAGS-85 showing additional structural characteristics in the XRD spectra. We find that the crystal structure of TAGS-85 is in the cubic phase (Fm-3m) rather than in the rhombohedral phase as normally observed in bulk TAGS-85. The difference between R3m GeTe and Fm-3m GeTe can be observed at the two-theta angles between 25–30° and 40–45°. Double peaks within this range are typical for R3m GeTe but they were not observed in our case. We think that the presence of the cubic structure might be due to the thin-film confinement as used in the present study. We also noticed that the peak positions are slightly shifted from the standard positions for Fm-3m GeTe. This is because TAGS-85 is just GeTe-rich but still with Ag and Sb dissolved. The XRD peaks of TAGS-50 can be matched with the cubic GeTe by carefully comparing it with the standard powder diffraction file cards. However, our APT results prove that the matrix composition is far away from stoichiometric GeTe composition and rather close to the nominal composition of TAGS-50 (50% GeTe and 50% AgSbTe_2) with slight Ag deficiency. Thus, we assign the peaks to the compound TAGS-50, which has also been studied by Oeckler et al.^[17] A small peak corresponding to the diamond Ge compound is also observed in both TAGS-50 and TAGS-85. Yet, it is still difficult to compare the volume fraction of this secondary phase due to the limited sensitivity of XRD when investigating NPs in general. To determine these secondary phases in TAGS-50 and TAGS-85, EDX investigations have been performed as described in Figure S1 and Table S1 in the Supporting Information. Although these EDX measurements allow the determination of the overall concentration for each constituent element, they do not identify

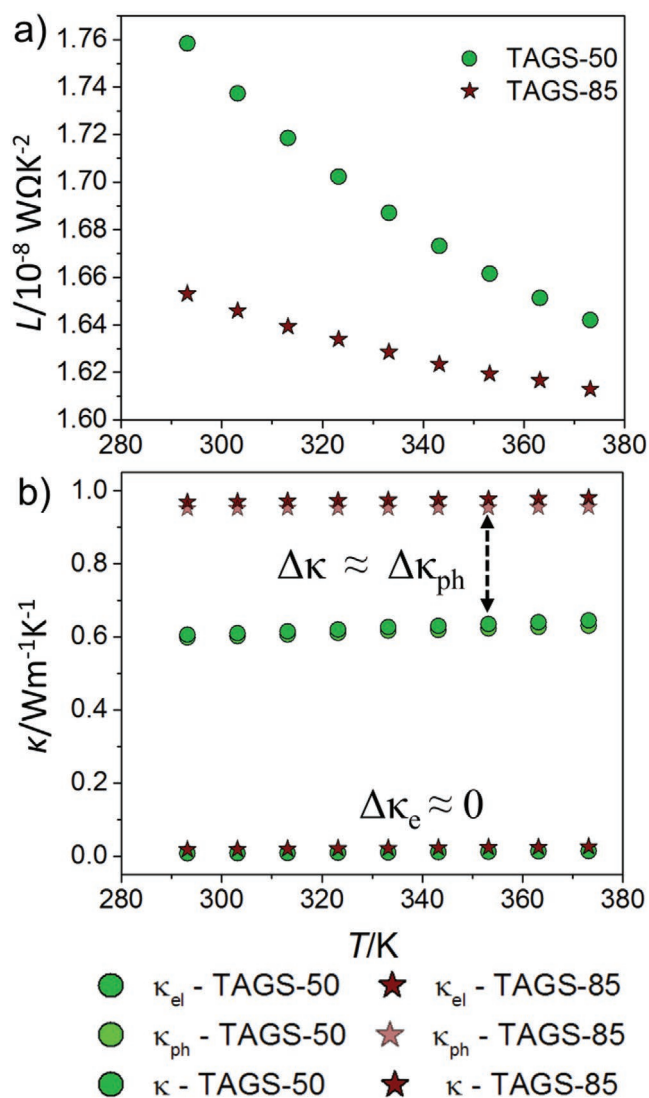


Figure 2. Thermal conductivity κ measured for TAGS-50 and TAGS-85 samples by the 3ω setup. While both samples exhibit a comparably low thermal conductivity, the thermal conductivity of TAGS-50 is lower by $\approx 35\%$ than the thermal conductivity of TAGS-85. Using the Lorenz number given in (a), the electronic component of the thermal conductivity κ_e was calculated. The value obtained is very low (see (b)), proving that the low thermal conductivity is mainly due to phonon scattering.

any precipitates in the TAGS-50 and TAGS-85 samples. Yet, these EDX measurements clearly show a certain deviation in Ag and Te concentrations from the expected nominal values, which might be related to the concentration inhomogeneities at very small length scales.

The thermal conductivities of TAGS-85 and TAGS-50 are plotted in **Figure 2** as a function of temperature. Both samples exhibit a very low thermal conductivity, comparable to other values reported in literature.^[17] Interestingly, the thermal conductivity is almost temperature independent. Hence, Umklapp scattering is not the dominant scattering mechanism for the phonons as usually observed in thermoelectric materials, since that would cause a T^{-1} change with increasing temperature.^[5] In contrast, the phonon scattering by defects is temperature

independent. Moreover, we have observed a clear reduction in thermal conductivity when going from TAGS-85 to TAGS-50. The electronic contribution of κ (κ_e) has been calculated using the Wiedemann–Franz law ($\kappa_e = L\sigma T$, where L is the Lorenz number given in Figure 2a calculated using the single parabolic band model, σ is the electrical conductivity, and T is the temperature) to verify that the reduction in κ is not mainly due to its electronic component κ_e . Figure 2b clearly shows that κ_e has only a very small effect on κ . Thus, the main effect is assigned to the lattice component κ_l . The goal of the current work is, hence, to understand the reasons behind this κ_l reduction. For that, TAGS-85 and TAGS-50 are further investigated down to the nanometer level using APT capabilities in order to identify the nature of the chemical inhomogeneities on the one hand and to relate these chemical inhomogeneities to the lattice thermal conductivity on the other hand.

APT measurements were performed to trace these compositional inhomogeneities at the nanometer level in TAGS-50 and TAGS-85 samples. The results obtained by APT are summarized in **Figures 3** and **4**. It has to be mentioned that the matrix composition at different laser powers was determined since a change in laser energy can result in a change of composition.

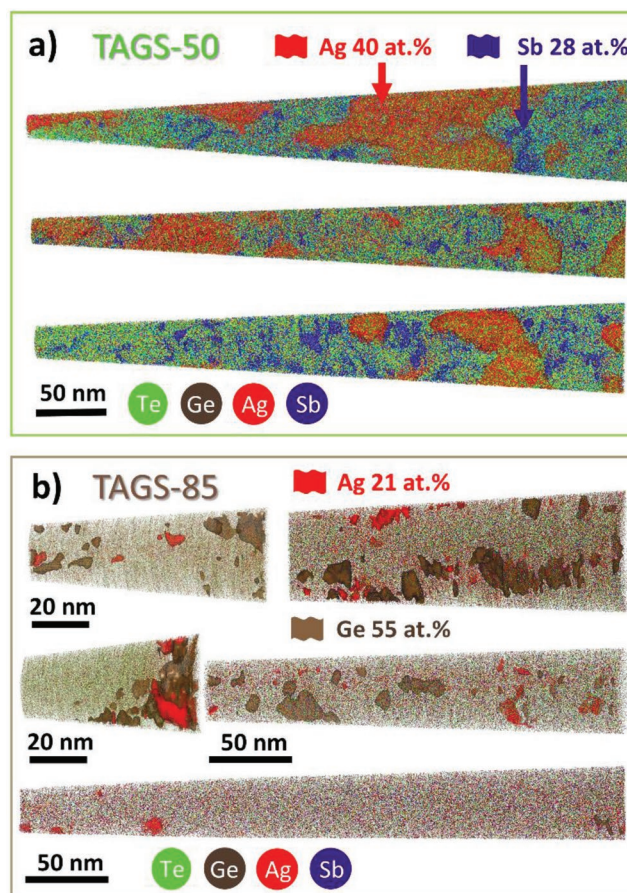


Figure 3. 3D APT maps of TAGS-50 and TAGS-85 revealing the existence of NPs. a) APT reconstruction of three different APT measurements performed on TAGS-50 demonstrating the presence of Ag and Sb-rich NPs. In contrast, in b) the APT reconstructions of five measurements on crystalline TAGS-85 we find only Ag and Ge-rich clusters.

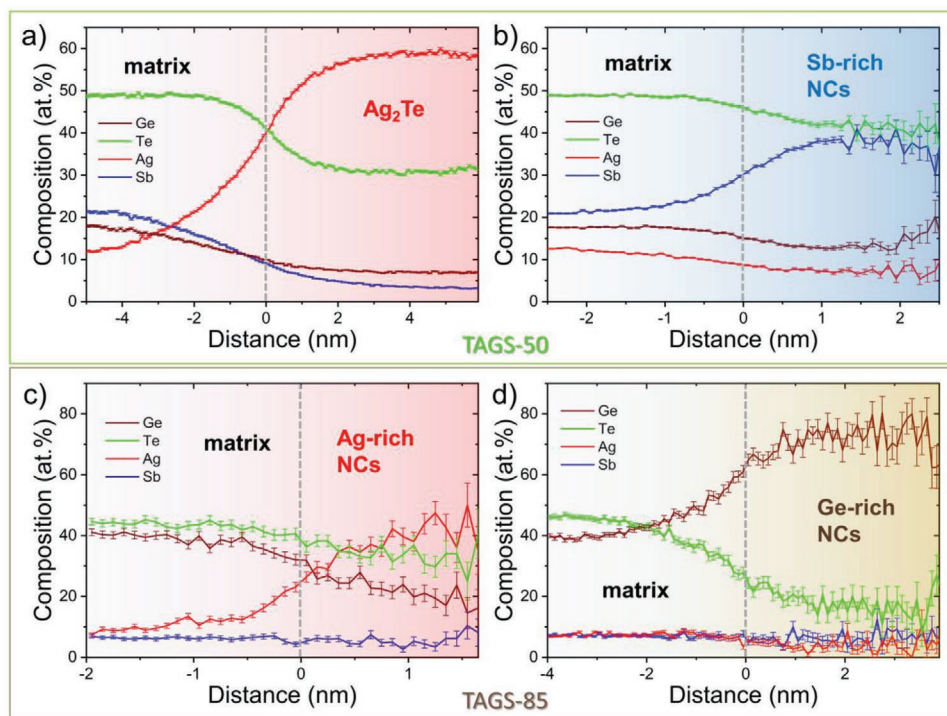


Figure 4. Composition of NPs and clusters in TAGS-50 and TAGS-85. In (a), the typical composition of the Ag_2Te NP (≈ 45 nm in diameter) containing ≈ 7 at% Ge and ≈ 4 at% Sb is given using the proximity histogram constructed based on an iso-composition value of 40 at% Ag. The same is shown in (b) and (c) but for Sb and Ag-rich clusters (NCs with 1–4 nm in diameter) using an iso-composition value of 28 at% Sb and 21 at% Ag. Contrary to (a), for these Ag and Sb-rich NCs no specific stable phase could be assigned. They correspond most probably to metastable phases. d) Ge-rich NPs (diameter ≈ 14 nm on average) containing a very high Ge concentration as shown by the proximity histogram generated using an iso-composition value of 55 at%.

More specifically, no change in the composition is observed within the applied laser energy range from 4 to 10 pJ for TAGS-50 and from 1 to 15 pJ for TAGS-85. These composition values can be found in Figure S2 in the Supporting Information. Moreover, the composition of the matrix obtained by APT deviates from that obtained by EDX because of strong chemical inhomogeneities observed at the nanoscale as described below.

For TAGS-50, Ag-rich NPs with a high volume fraction of 0.32 are detected as highlighted in Figure 3a by the red iso-composition surface of 40 at% Ag. The exact structural and chemical characteristics averaged over all NPs detected are given in Table 1. The composition of these Ag-rich NPs is also depicted in a proximity histogram (called also proxigram) found in Figure 4a. These APT results suggest the presence of Ag_2Te phase highly doped with Ge and Sb in TAGS-50. Even though the concentration of Ag is slightly lower than the nominal concentration for the Ag_2Te phase, the total concentration of cations is about 69 at%, suggesting that these NPs correspond to the Ag_2Te phase. Similar Ag_2Te NPs have also been found in TAGS bulk materials. For example, Kim et al. observed Ag_2Te pre-

cipitates in TAGS prepared by ball milling and spark plasma sintering.^[26] Moreover, Figures 3a and 4b reveal also the presence of tiny Sb-rich clusters highlighted by the blue iso-composition surface of 28 at% Sb. These clusters have a diameter of only 5–7 nm (on average), which is much smaller than that calculated for Ag_2Te NPs (i.e., 45 nm, see Table 1). Fur-

Table 1. Structure and composition of Ag_2Te and Ge NPs in TAGS-50 and TAGS-85 averaged over all measured APT specimens. Structural characteristics, such as volume fraction (volume NPs/total volume), interface area (nm^2), and interface area/volume (nm^{-1}), as well as the average composition (at%), is given for the Ag_2Te and Ge-rich NPs. Moreover, the size of these NPs is given by the product $h \times d$, where h is the height and d is the diameter (not fully spherical).

Nanoprecipitates (NPs)	Average size: $h \times d$ [nm]	Volume fraction	Average composition [at%]	Interface area [$10^4 \times \text{nm}^2$]	Interface area/volume [$10^{-2} \times \text{nm}^{-1}$]
Ag_2Te -NPs (TAGS-50)	36×50	0.32	Ag: 58 ± 1	7.9	1.6
			Te: 31 ± 0.9		
			Ge: 7 ± 0.5		
			Sb: 4 ± 0.5		
Ge-rich NPs (TAGS-85)	8×12	0.13	Ge: 75 ± 1	1.5	0.9
			Te: 15.5 ± 0.8		
			Sb: 6 ± 0.5		
			Ag: 2.5 ± 0.4		

ther structural and chemical characteristics of these clusters are given in Table S2 in the Supporting Information. Contrary to the Ag_2Te NPs, no stable phase could be assigned to the Sb-rich clusters because of their complex elemental composition.^[27] They most probably correspond to metastable phases formed during annealing. Another interesting feature is the Ag_2Te /matrix interface area calculated for all APT datasets. Specifically, a very large interface area of $7.9 \times 10^4 \text{ nm}^2$ was calculated for a total volume of $5 \times 10^6 \text{ nm}^3$, much larger than that calculated for the Sb-rich NCs/matrix interface (Table S2, Supporting Information).

Contrary to TAGS-50, Ge-rich NPs are observed in TAGS-85 as highlighted by the 3D APT maps from Figures 3b and 4d in agreement with Davidow and Gelbstein, who proved the existence of Ge- and Ag-rich secondary phases in bulk TAGS-85 prepared by hot pressing.^[16] These APT results clearly show that these Ge-rich NPs are tiny (average diameter of only 14 nm) with a small volume fraction of only 0.13 (see Table 1). Moreover, the distribution of NPs is found to be inhomogeneous throughout the material. For example, the fifth measurement shows only sporadic NPs compared with the other four measurements. The Ge content in the Ge-rich NPs reaches values between 70 and 80 at%, while Te, Sb, and Ag compositions are diminished compared to the matrix composition with values ranging from 12 to 20 at% for Te, from 4 to 8 at% for Sb, and from 2 to 4 at% for Ag, respectively. This implies that the Ge precipitate is supersaturated with Te, Sb, and Ag. The average composition is given in Table 1, while Figure 4d depicts the composition of one of the Ge-rich NPs. Besides the Ge phase, these composition values might also suggest the presence of $\text{Ag}_2\text{Ge}_{85}\text{SbTe}_{10}$ as suggested by Perumal et al.^[28] for TAGS-85.

No Ag_2Te NPs are observed in TAGS-85, but instead tiny Ag-rich clusters (few nm in diameter, see Figures 3b and 4c) are detected. Beside one Ag-pure cluster ($96.5 \pm 2 \text{ at\% Ag}$ and $1.9 \pm 0.2 \text{ at\% Sb}$), all the other clusters contain on average $29 \pm 0.9 \text{ at\% Ag}$, $7 \pm 0.5 \text{ at\% Sb}$, $26 \pm 0.8 \text{ at\% Ge}$, and $38 \pm 1 \text{ at\% Te}$ (see Table S2, Supporting Information). Based on the measured compositions by APT, no stable phase could be assigned to these tiny Ag-rich clusters. Moreover, their volume fraction is even smaller than that of Ge NPs (0.03 compared to 0.13, see Table 1 and Table S2, Supporting Information) suggesting that their impact on the thermal conductivity might be very small.

The matrix/Ge NP interface area is only $1.5 \times 10^4 \text{ nm}^2$ calculated in a volume of $1.6 \times 10^6 \text{ nm}^3$. This corresponds to an interface area/volume of 0.009 nm^{-1} , which is larger than that calculated for the Ag-rich clusters/matrix interface (0.005 nm^{-1} , see Table S2, Supporting Information). Yet this value is almost two times smaller than the value calculated for the matrix/ Ag_2Te NP interface in TAGS-50 (interface area/volume equal to 0.016 nm^{-1} , see Table 1).

Not only striking differences in nanoprecipitation have been observed between TAGS-50 and TAGS-85, but also in bond breaking behavior observed during the APT experiments. To field evaporate the atoms from the apex of the needle-shaped specimen, the bonds first need to break from the surface and then the ionized atoms can be evaporated. In the present work, it has been found that a high probability of multiple events (PME) of $\geq 60\%$ (see Figure 5 where multiple event is defined as more than one ion detected per effective laser pulse) is detected for the matrix of both stoichiometries and for the Sb-rich clusters (observed in TAGS-50), whereas a low PME

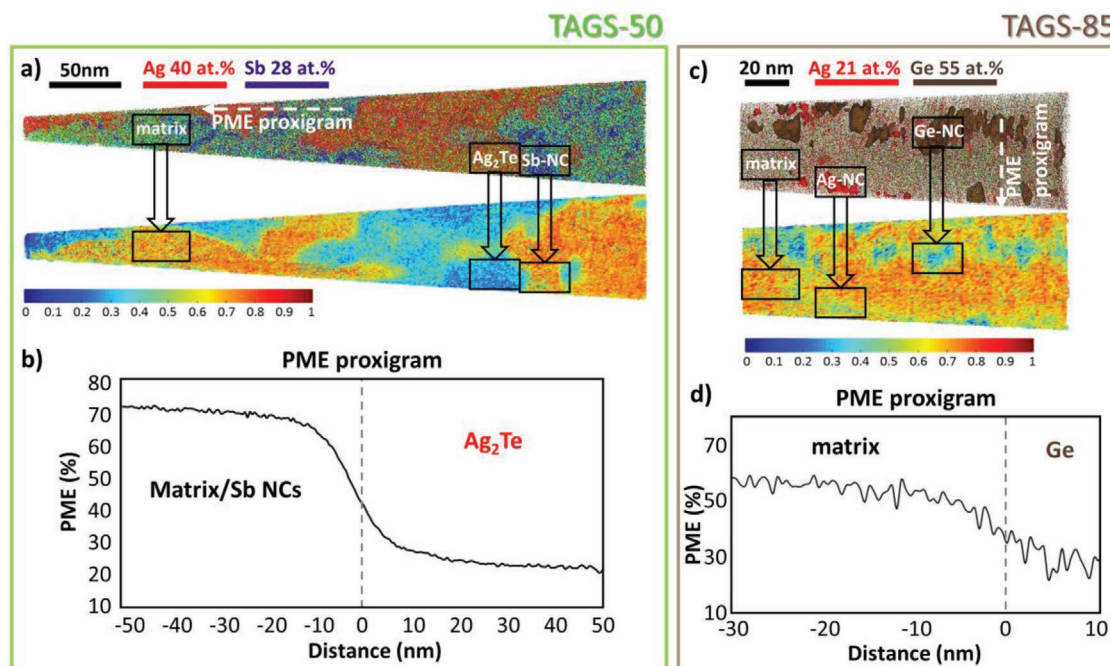


Figure 5. Probability for multiple events of a) TAGS-85 and b) TAGS-50. The regions of low probability for multiple events ($\text{PME} \leq 30\%$) correspond to Ag_2Te (TAGS-50) and Ge NPs (TAGS-85). On the contrary, regions of high probability for multiple events ($>60\%$) correspond to both the matrix and the Sb-rich clusters. The PME proxigram clearly exhibits a strong variation in PME when crossing the interface between the matrix and Ag_2Te for TAGS-50 or the matrix and Ge for TAGS-85. We note here that the Ag-rich clusters (NCs) for TAGS-85 show an intermediate value of $\approx 40\%$ for PME.

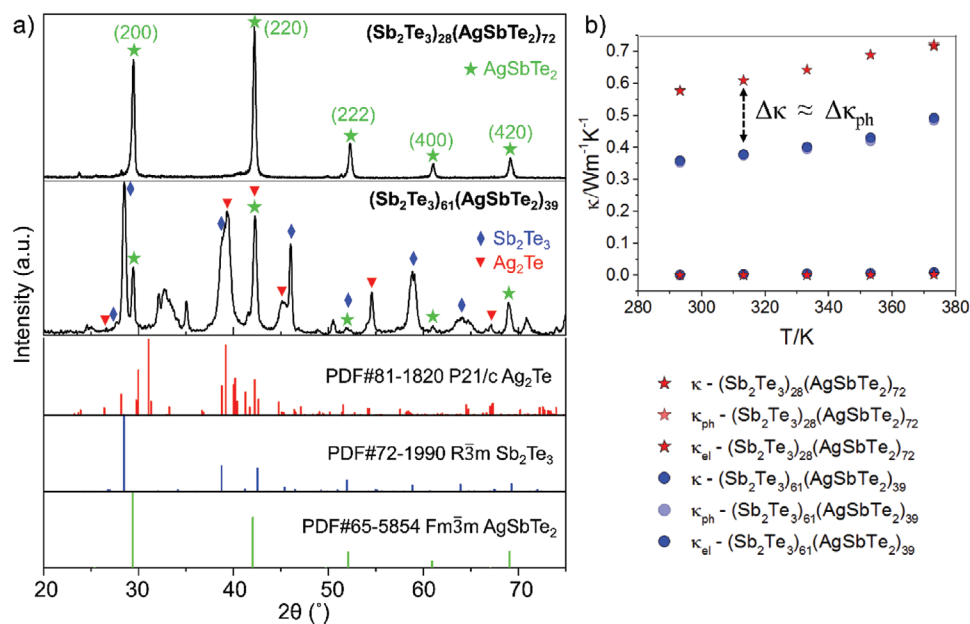


Figure 6. a) Grazing incidence XRD measurements of $(\text{Sb}_2\text{Te}_3)_{28}(\text{AgSbTe}_2)_{72}$ and $(\text{Sb}_2\text{Te}_3)_{61}(\text{AgSbTe}_2)_{39}$. The green stars represent the AgSbTe_2 phase, while the blue diamonds and the red triangles represent the Sb_2Te_3 and Ag_2Te phases, respectively. The $(\text{Sb}_2\text{Te}_3)_{28}(\text{AgSbTe}_2)_{72}$ sample exhibits a perfect AgSbTe_2 structure, whereas the $(\text{Sb}_2\text{Te}_3)_{61}(\text{AgSbTe}_2)_{39}$ sample exhibits the presence of not only the expected AgSbTe_2 phase but also of Sb_2Te_3 and Ag_2Te phases. b) Thermal conductivity κ measured for $(\text{Sb}_2\text{Te}_3)_{28}(\text{AgSbTe}_2)_{72}$ and $(\text{Sb}_2\text{Te}_3)_{61}(\text{AgSbTe}_2)_{39}$ samples. While both samples exhibit a comparably low thermal conductivity, the thermal conductivity κ and the corresponding lattice thermal conductivity κ_l of $(\text{Sb}_2\text{Te}_3)_{61}(\text{AgSbTe}_2)_{39}$ is lower by $\approx 42\%$ than the ones of $(\text{Sb}_2\text{Te}_3)_{28}(\text{AgSbTe}_2)_{72}$.

($\leq 30\%$, see Figure 5) is observed for Ag_2Te (for TAGS-50) and Ge (for TAGS-85) NPs. These results are in-line with recent work where it had been proven that main-group chalcogenide thermoelectric materials exhibit systematically a high PME of $\geq 60\%$.^[8,29]

To consolidate the consistency of the results shown above another similar system, namely, $(\text{Sb}_2\text{Te}_3)_x(\text{AgSbTe}_2)_{(1-x)}$ had been investigated. For simplicity, only two stoichiometries will be described here: $(\text{Sb}_2\text{Te}_3)_{61}(\text{AgSbTe}_2)_{39}$ and $(\text{Sb}_2\text{Te}_3)_{28}(\text{AgSbTe}_2)_{72}$. **Figure 6** summarizes the XRD and thermal conductivity results, while Figures S3–S6 in the Supporting Information summarize the TEM and APT results obtained for these two stoichiometries.

The grazing incidence XRD measurements show that the $(\text{Sb}_2\text{Te}_3)_{28}(\text{AgSbTe}_2)_{72}$ sample exhibits a AgSbTe_2 structure, whereas the $(\text{Sb}_2\text{Te}_3)_{61}(\text{AgSbTe}_2)_{39}$ sample exhibits the presence of not only the expected AgSbTe_2 phase but also of Sb_2Te_3 and Ag_2Te phases. These observations agree well with the thermal conductivity κ measurements and with our previous example. Namely, the lattice thermal conductivity κ_l of $(\text{Sb}_2\text{Te}_3)_{61}(\text{AgSbTe}_2)_{39}$ sample, containing Ag_2Te NPs characterized by low-PME value, is lower by $\approx 42\%$ than the one of $(\text{Sb}_2\text{Te}_3)_{28}(\text{AgSbTe}_2)_{72}$ sample for which no such precipitates were detected neither by TEM nor by APT.

The high PME value observed systematically for chalcogenide thermoelectric materials is attributed to MVB.^[8] The existence of MVB in TAGS is further verified by the optical dielectric constant ϵ_∞ given in **Figure 7**. One of the established property-based fingerprints for MVB is the optical dielectric constant ϵ_∞ , which is an optical identifier and can be measured by Fourier-transform infrared spectroscopy (FTIR). For

amorphous TAGS- x materials the measured ϵ_∞ values are low (≈ 15) in agreement with Wuttig et al.^[24] Yet, the crystalline TAGS- x materials show much higher values (>30) than their amorphous counterparts for stoichiometries investigated along the pseudo-binary line GeTe-AgSbTe_2 . This pronounced increase of ϵ_∞ upon crystallization cannot be attributed to the modest density increase of less than 9%, which is shown in Figure 7c. According to the Clausius–Mossotti relation, the contrast comes from a strong enhancement of the bond polarizability upon crystallization, which is attributed to MVB.^[24,30] Based on the APT and FTIR measurements, we conclude that crystalline TAGS- x compounds adopt MVB. This demonstrates that MVB can also exist in I–V–VI₂ chalcogenides and related alloys. This indicates that there could be many more materials utilizing such a bonding mechanism, beyond the previously identified V, VI, IV–VI, and V₂VI₃ compounds as well as their alloys^[8] as already recently evidenced in studies of V₂VI₃ compounds.^[31]

Moreover, the ϵ_∞ value of crystalline TAGS-85 is 10% larger than that of crystalline TAGS-50. This can be explained by the fact that the volume fraction of the matrix (MVB material) for TAGS-85 is larger than that for TAGS-50 as highlighted in Figure 5 (0.84 for TAGS-85 instead of 0.62 for TAGS-50).

It had been argued that octahedrally coordinated chalcogenide thermoelectric materials such as PbTe and PbS are characterized by an intrinsic low lattice thermal conductivity κ_l due to their large anharmonicity,^[8] i.e., anharmonic phonon scattering by Umklapp and Normal processes. Apparently this also holds for AgSbTe_2 and its alloys with GeTe . This explains why both stoichiometries, TAGS-50 and TAGS-85, possess low lattice thermal conductivities. Yet, the lattice thermal

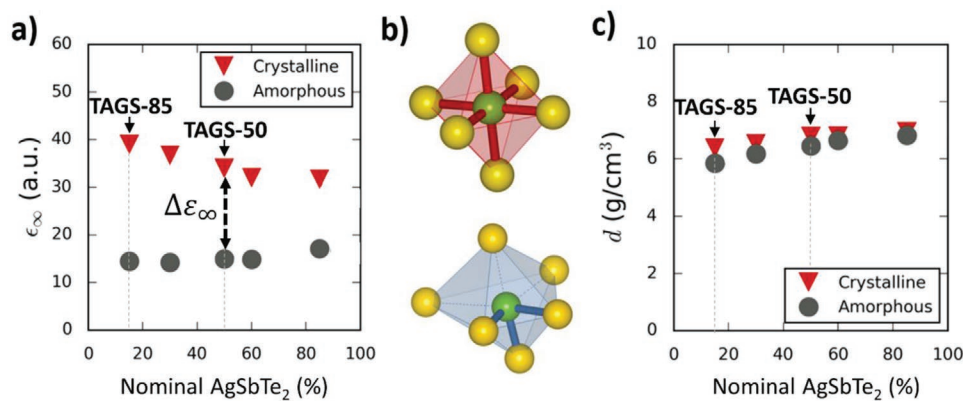


Figure 7. Proof of existence of MVB in TAGS. a) Optical dielectric constant ϵ_{∞} as a function of stoichiometry in the amorphous and crystalline phases. ϵ_{∞} exhibits much larger values in the crystalline phase as compared to the amorphous phase. The increase of ϵ_{∞} upon crystallization can be attributed to the transition from b) covalent bonding (amorphous phase) to MVB (crystalline phase). c) Mass density d as a function of stoichiometry in the amorphous and the crystalline phases. The change in d upon crystallization cannot account for the large increase in ϵ_{∞} . The latter is therefore attributed to a strong enhancement in the bond polarizability, according to the Clausius–Mossotti relation, ascribed to the transition from covalent to MVB.

conductivity κ_l for TAGS-50 is clearly 35% lower than that of TAGS-85.

The 3D PME maps from Figure 5 obtained using EPOSA software^[32] clearly show the distribution of the low PME regions (NPs) in a high PME matrix. The volume fraction of the low PME regions in TAGS-50, which corresponds to Ag₂Te NPs with a volume fraction of 0.32, is considerably higher than that determined for TAGS-85 (Ge NPs with a volume fraction of only 0.13). Moreover, the interface area/volume ratio for the matrix (MVB)/Ag₂Te (non-MVB) interface in TAGS-50 is 0.016 nm⁻¹, which is much higher than that measured for TAGS-85 (0.009 nm⁻¹ calculated for the matrix/Ge interface).

The intrinsic lattice thermal conductivity of AgSbTe₂ and GeTe is about 0.7 and 2.6 W mK⁻¹, respectively.^[33,34] Intuitively, it might be normal to expect a lower lattice thermal conductivity with increasing the content of AgSbTe₂ in the TAGS system. However, the κ_l value at room temperature for TAGS-75, TAGS-80, and TAGS-85 was reported to be 0.8, 0.6, and 0.7 W mK⁻¹, respectively.^[28] TAGS-75 has a higher content of AgSbTe₂ (lower content of GeTe) but exhibits also a higher value of κ_l . This indicates that the high content of AgSbTe₂ might not be the key ingredient of low lattice thermal conductivity. Another example can be found in the (GeTe)_x(AgSbSe₂)_(1-x) system. Similar to AgSbTe₂, AgSbSe₂ has also an intrinsically low lattice thermal conductivity due to the large anharmonicity. Samanta et al.^[34] reported that the lattice thermal conductivity is minimized in the compound with 20 at% AgSbSe₂. Adding more AgSbSe₂ oppositely increases the lattice thermal conductivity. The measured lattice thermal conductivity in this work is 0.95 and 0.6 W mK⁻¹ for TAGS-85 and TAGS-50, respectively. Hence, this appreciable decrease of lattice thermal conductivity in TAGS-50 cannot be simply ascribed to the increased content of AgSbTe₂.

Tan et al.^[35] had recently discussed the effect of adding Cd into SnTe on its thermoelectric properties. They showed that two effects take place. The first effect is to promote the band convergence by increasing the band gap and decreasing the energy separation between L and Σ valence bands. The other effect is to introduce CdS precipitates for enhancing the phonon scattering; the effect which is studied in the present work. Very

recently, a novel approach has been introduced to realize a huge phonon scattering process by incorporating CdTe-coated layers on the surface of SnTe grains.^[36] The authors explained that such scattering is induced by the acoustic impedance mismatch between the CdTe-coated layer and the SnTe grain. Interestingly, in all these examples the matrix is an MVB material, whereas the nanostructure is a non-MVB material, more specifically a covalently bonded material. Hence, the scattering of phonons at interfaces has to be explored. For phonons to scatter at a heterointerface, the phonon frequency spectrum at this specific heterointerface should change significantly. The phonon frequencies in solids can be demonstrated based on a simple model of semi-infinite 1D chains of reduced masses (M) connected by springs with a force constant K , which depends upon the interatomic coupling, i.e., the chemical bond between adjacent atoms.^[37] The phonon dispersion is directly related to the value of $\sqrt{K/M}$. A change of the ratio K/M causes the mismatch of phonon dispersions and thus the phonon scattering. Therefore, significant scattering of phonons at interfaces can be realized by utilizing compounds with a significant variation in the reduced masses of the atoms involved and/or with distinct chemical bonding across the interface. If both the reduced masses and the chemical bonding mechanism are very similar, i.e., similar value for K/M , the effective phonon scattering by interface could be marginal. For example, He et al.^[38] observed a very high density of NPs (10¹¹ cm⁻²) in Na/K-doped PbTe but these NPs (Na/K-rich PbTe) did not contribute appreciably to the reduction in lattice thermal conductivity. This is due to the similar reduced masses and the same chemical bonding mechanism between the existing precipitates and the matrix. On the contrary, the PbS precipitates in a PbTe matrix scatter phonons effectively^[39] because of their very different reduced masses knowing that both phases adopt MVB according to Yu et al.^[8] In this work, the reduced masses for Ag₂Te precipitates and TAGS-50 matrix are very close but the force constants are very different. Our previous work summarized that all the MVB compounds embrace very low Debye temperature and low bulk modulus, which are indicative of a soft chemical bond. However, the covalent bond is known to

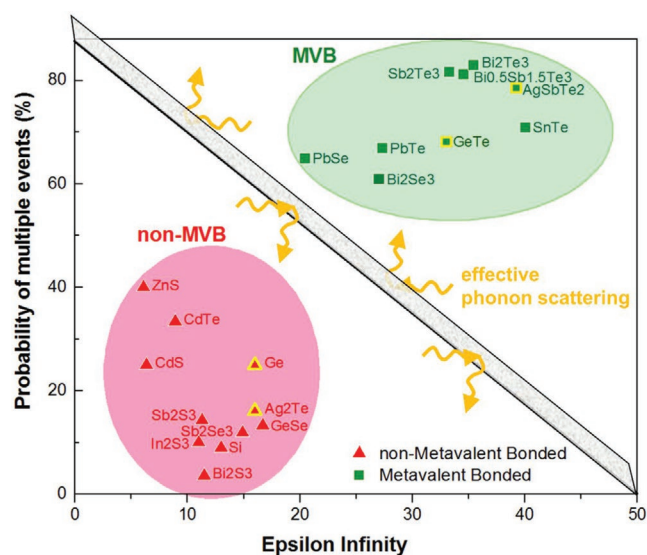


Figure 8. ϵ_{∞} versus the probability of multiple events (PME) measured by laser-assisted APT. All the compounds with a high PME value are located in the green area of the map. Most of these compounds are used as thermoelectrics and are characterized by unconventional properties, such as high dielectric constants and transverse optical Grüneisen parameter ($\gamma_{TO} > 2$) as well as low thermal conductivities (see Table S3 in the Supporting information). Moreover, the green area corresponds also to materials which exhibit MVB, called MVB materials in the present work. In the red region, the PME values are low ranging from about 4% to more than 35%. The materials from this region are neither intrinsically good thermoelectrics nor MVB materials, being called non-MVB materials in this work. The data points marked by a yellow frame are obtained from the present work, whereas the other points are taken from literature.^[8,31,40a,b]

be much stronger than MVB.^[8] Thus, the observed decrease in lattice thermal conductivity should stem from the difference in the force constants, which is directly related to the chemical bonding. This work implies that phonon scattering at interfaces depends very much upon the change in reduced masses or in chemical bonding of the materials involved to have considerable mismatches for the K/M ratio at the interface.

Hence, the present results on $(\text{GeTe})_x(\text{AgSbTe}_2)_{(1-x)}$ and $(\text{Sb}_2\text{Te}_3)_x(\text{AgSbTe}_2)_{(1-x)}$ systems together with the existing results from literature are summarized in **Figure 8** where two distinctive classes of materials are highlighted. All the thermoelectric materials characterized by a high PME value ($>50\%$) and a high optical dielectric constant ϵ_{∞} (>25 , except for PbSe) are localized in the green region. These materials are coined MVB materials, since they exhibit MVB.^[8,24,31] On the contrary, the materials in the red regions are characterized by a low PME value ($<38\%$) and a low ϵ_{∞} value (<18). They are called non-MVB materials since they exhibit covalent bonding. Hence, this work implies that the phonons are effectively scattered by such MVB/non-MVB heterointerfaces as sketched in **Figure 8**. Furthermore, this figure gives hints about other possible MVB/non-MVB heterointerfaces such as $\text{Bi}_2\text{Te}_3/\text{CdTe}$, PbTe/CdTe , SnTe/CdTe , and PbSe/GeSe heterointerfaces, which can effectively scatter phonons as well.

Another important aspect for thermoelectric material design is the area/volume fraction of MVB/non-MVB heterointerfaces. Yet, determining the impact of the area/volume fraction of such

interfaces on the thermal conductivity directly in a bulk material can be a real challenge (very often inhomogeneous material structure and composition in all three dimensions).^[20] One of the advantages of the present work is the deposition of TAGS- x thermoelectric as a thin-film^[41] allowing us to better confine the scattering processes in the TAGS- x material and to better correlate the existing NPs with the lattice thermal conductivity κ_l allowing, thus, an easier verification of our experimental proof-of-principle. Finally, the present study implies that the lattice thermal conductivity κ_l can be inhibited by introducing interfaces with different chemical bonding mechanism in addition to controlling the composition, size, and morphology of precipitates. Hence, the higher MVB/non-MVB interface area/volume ratio determined for TAGS-50 than TAGS-85 (0.32 vs 0.13) could be a very plausible reason for the reduced lattice thermal conductivity κ_l in TAGS-50 as compared to TAGS-85.

3. Conclusion

In conclusion, the present work demonstrates that the TAGS-50 sample, which exhibits the lowest thermal conductivity, contains a high density of Ag-based NPs approaching the composition of Ag_2Te phase. Such precipitates are absent in TAGS-85. Instead, a nonnegligible volume fraction of Ge NPs was determined. Other tiny clusters, such as Sb-rich and Ag-rich clusters, are detected in TAGS-50 and TAGS-85, respectively. This example on TAGS- x was consolidated by a second study performed on $(\text{Sb}_2\text{Te}_3)_x(\text{AgSbTe}_2)_{(1-x)}$. Here, the same was observed, i.e., the stoichiometry containing the Ag_2Te NPs is the one which exhibits the lowest thermal conductivity. Moreover, using the 3D PME map extracted from APT data, we could clearly differentiate the materials with covalent bonds (such as Ag_2Te) from those with MVB (such as matrix and Sb-rich clusters). Moreover, it has been proven quantitatively that a large interface area/volume of non-MVB/MVB interfaces is beneficial to reduce the lattice thermal conductivity via phonon-interface scattering. Hence, the present study shows the impact of NPs with different bonding mechanisms on the thermal conductivity of TAGS- x thermoelectric materials with a particular emphasis on the Ag_2Te -matrix interface.

4. Experimental Section

Sample Preparation and Standard Characterization: $(\text{GeTe})_x(\text{AgSbTe}_2)_{1-x}$ alloys with varying composition were deposited from stoichiometric GeTe and AgSbTe₂ targets by DC magnetron co-sputtering (background pressure 2×10^{-6} mbar, Ar flow 20 sccm, deposition rate $<1 \text{ \AA s}^{-1}$). The as-deposited amorphous films were annealed for 30 min at 250 °C under Ar atmosphere to obtain nonoriented polycrystalline samples. Crystallization of the thin films was confirmed by XRD using a Bruker D8 Discover setup equipped Cu X-ray source with a Goebel mirror and a two-bounce Ge (220) ACC monochromator. Stoichiometry and density were determined by EDX and X-ray reflectometry respectively, performed on 120 nm thin films deposited on silicon substrate.

Thermal Conductivity Measurements: The thermal conductivities of the two TAGS- x samples with compositions of $x = 85\%$ and $x = 50\%$ (denominated TAGS-85 and TAGS-50) were measured by means of a custom-built 3ω setup.^[42] To perform the measurement, 650 nm thin films deposited onto a silicon substrate were capped by a 100 nm dielectric film of $(\text{ZnS})_{80}(\text{SiO}_2)_{20}$ by radio frequency magnetron sputtering deposition. Subsequently, 100 nm aluminum wires were

deposited on top of the dielectric layer; the wire geometry was defined by applying a patterned mask through photolithography prior to deposition. The resulting sample geometry was described previously.^[43]

Chemical Characterization at the Nanoscale: APT specimens were prepared by applying the in situ lift-out method and annular milling^[44] using the dual beam Helios Nanolab from FEI. The Ga ion-milling process was finalized by a low-energy (5 kV) cleaning step to prevent specimen damage by Ga⁺ implantation. APT measurements were conducted using a CAMECA LEAP 4000X Si, with a laser wavelength of 355 nm (UV), a pulse duration of 10 ps, pulse frequency of 250 KHz, detection rate of 0.5%, and laser pulse energies between 1 and 15 pJ at a base temperature of 40 K.

Structural Characterization at the Nanoscale: TEM lamellae were prepared by applying the standard in situ lift-out method using the dual beam Helios Nanolab from FEI. TEM experiments were then conducted to determine the structure of the (Sb₂Te₃)_x(AgSbTe₂)_(1-x) films using a TEM setup (FEI Titan) operating at 300 keV.

Measurement of Dielectric Constant: For FTIR measurements, 650 nm thin films were sputtered on a glass substrate covered by 150 nm of aluminum. The thickness of the films was determined on reference samples by Bruker DektakXT stylus profiler. Room-temperature reflectance spectra from 400 to 8000 cm⁻¹ were recorded using a Bruker IFS 66v/S spectrometer. The optical response of the TAGS film was modeled with the following dielectric function^[30]

$$\epsilon(\omega) = \epsilon_{\text{const}} + \epsilon_{\text{Tauc-Lorentz}}(\omega; \omega_0, S, \gamma, \omega_g) + \epsilon_{\text{Drude}}(\omega; \omega_p, \omega_d) \quad (1)$$

where ϵ_{const} is a constant that accounts for the polarizability in the higher energy range, $\epsilon_{\text{Tauc-Lorentz}}$ describes the onset of optical transitions, and $\epsilon_{\text{Drude}}(\omega)$ is the contribution of free carriers. ϵ_{∞} is given by

$$\epsilon_{\infty} = \lim_{\omega \rightarrow 0} [\epsilon(\omega) - \epsilon_{\text{Drude}}(\omega; \omega_p, \omega_d)] \quad (2)$$

[Further details of the crystal structure investigation(s) may be obtained from the Fachinformationszentrum Karlsruhe, 76344 Eggenstein-Leopoldshafen (Germany), on quoting the depository number CSD- sd_0305051].

Supporting Information

Supporting Information is available from the Wiley Online Library or from the author.

Acknowledgements

The authors thank Sebastian Mohrhenh and Mohit Raghuwanshi for technical and experimental support as well as for the fruitful discussions. This project was realized within the SFB 917 Nanoswitches and the RWTH Seeds Funds 2017.

Conflict of Interest

The authors declare no conflict of interest.

Keywords

interface scattering, multivalent bonding, nanoprecipitates, thermal conductivity, thermoelectrics

Received: December 2, 2019

Revised: January 10, 2020

Published online: February 28, 2020

- [1] G. J. Snyder, E. S. Toberer, *Nat. Mater.* **2008**, *7*, 105.
- [2] J. R. Sootsman, D. Y. Chung, M. G. Kanatzidis, *Angew. Chem., Int. Ed.* **2009**, *48*, 8616.
- [3] G. S. Nolas, G. A. Slack, S. B. Schujman, in *Recent Trends in Thermoelectric Materials Research I*, Vol. 69 (Ed: T. M. Tritt), Elsevier, New York **2001**, pp. 255–300.
- [4] X. Shi, L. Chen, C. Uher, *Int. Mater. Rev.* **2016**, *61*, 379.
- [5] E. S. Toberer, A. Zevalkink, G. J. Snyder, *J. Mater. Chem.* **2011**, *21*, 15843.
- [6] M. D. Nielsen, V. Ozolins, J. P. Heremans, *Energy Environ. Sci.* **2013**, *6*, 570.
- [7] S. Lee, K. Esfarjani, T. Luo, J. Zhou, Z. Tian, G. Chen, *Nat. Commun.* **2014**, *5*, 3525.
- [8] Y. Yu, M. Cagnoni, O. Cojocar-Mirédin, M. Wuttig, *Adv. Funct. Mater.* **2019**, 1904862, <https://doi.org/10.1002/adfm.201904862>.
- [9] Y. Yu, D.-S. He, S. Zhang, O. Cojocar-Mirédin, T. Schwarz, A. Stoffers, X.-Y. Wang, S. Zheng, B. Zhu, C. Scheu, D. Wu, J.-Q. He, M. Wuttig, Z.-Y. Huang, F.-Q. Zu, *Nano Energy* **2017**, *37*, 203.
- [10] C. Zhou, Y. Yu, Y. K. Lee, O. Cojocar-Mirédin, B. Yoo, S.-P. Cho, J. Im, M. Wuttig, T. Hyeon, I. Chung, *J. Am. Chem. Soc.* **2018**, *140*, 15535.
- [11] Y. Yu, C. Zhou, S. Zhang, M. Zhu, M. Wuttig, C. Scheu, D. Raabe, G. J. Snyder, B. Gault, O. Cojocar-Mirédin, *Mater. Today* **2019**, <https://doi.org/10.1016/j.mattod.2019.11.010>.
- [12] J. Yang, T. Caillat, *MRS Bull.* **2006**, *31*, 224.
- [13] C. Wood, *Rep. Prog. Phys.* **1988**, *51*, 459.
- [14] E. A. Skrabek, D. S. Trimmer, *US* **3,945,855**, **1976**.
- [15] B. A. Cook, M. J. Kramer, X. Wei, J. L. Harringa, E. M. Levin, *J. Appl. Phys.* **2007**, *101*, 053715.
- [16] J. Davidow, Y. Gelbstein, *J. Electron. Mater.* **2013**, *42*, 1542.
- [17] T. Schröder, T. Rosenthal, N. Giesbrecht, M. Nentwig, S. Maier, H. Wang, G. J. Snyder, O. Oeckler, *Inorg. Chem.* **2014**, *53*, 7722.
- [18] Y. Tang, Z. M. Gibbs, L. A. Agapito, G. Li, H.-S. Kim, M. B. Nardelli, S. Curtarolo, G. J. Snyder, *Nat. Mater.* **2015**, *14*, 1223.
- [19] S. H. Yang, T. J. Zhu, T. Sun, J. He, S. N. Zhang, X. B. Zhao, *Nanotechnology* **2008**, *19*, 245707.
- [20] O. Cojocar-Mirédin, L. Abdellaoui, M. Nagli, S. Zhang, Y. Yu, C. Scheu, D. Raabe, M. Wuttig, Y. Amoyal, *ACS Appl. Mater. Interfaces* **2017**, *9*, 14779.
- [21] a) K. Biswas, J. He, I. D. Blum, C. I. Wu, T. P. Hogan, D. N. Seidman, V. P. Dravid, M. G. Kanatzidis, *Nature* **2012**, *489*, 414; b) J. He, I. D. Blum, H.-Q. Wang, S. N. Girard, J. Doak, L.-D. Zhao, J.-C. Zheng, G. Casillas, C. Wolverton, M. Jose-Yacamán, D. N. Seidman, M. G. Kanatzidis, V. P. Dravid, *Nano Lett.* **2012**, *12*, 5979; c) A. Sheskin, T. Schwarz, Y. Yu, S. Zhang, L. Abdellaoui, B. Gault, O. Cojocar-Mirédin, C. Scheu, D. Raabe, M. Wuttig, Y. Amoyal, *ACS Appl. Mater. Interfaces* **2018**, *10*, 38994.
- [22] a) Y. Yu, W. Zhu, X. Kong, Y. Wang, P. Zhu, Y. Deng, *Front. Chem. Sci. Eng.* **2019**, <https://doi.org/10.1007/s11705-019-1829-9>; b) I. Chowdhury, R. Prasher, K. Lofgreen, G. Chrysler, S. Narasimhan, R. Mahajan, D. Koester, R. Alley, R. Venkatasubramanian, *Nat. Nanotechnol.* **2009**, *4*, 235.
- [23] J. H. Kiely, D.-H. Lee, *Meas. Sci. Technol.* **1997**, *8*, 661.
- [24] M. Wuttig, V. L. Deringer, X. Gonze, C. Bichara, J.-Y. Raty, *Adv. Mater.* **2018**, *30*, 1803777.
- [25] J.-Y. Raty, M. Schumacher, P. Golub, V. L. Deringer, C. Gatti, M. Wuttig, *Adv. Mater.* **2019**, *31*, 1806280.
- [26] H.-S. Kim, P. Dharmiah, B. Madavali, R. Ott, K.-H. Lee, S.-J. Hong, *Acta Mater.* **2017**, *128*, 43.
- [27] H. Okamoto, in *Binary Alloy Phase Diagrams*, Vol. 2 (Ed: T. B. Massalski), ASM International, Materials Park, OH **1990**, pp. 3308–3310.
- [28] S. Perumal, S. Roychowdhury, K. Biswas, *J. Mater. Chem. C* **2016**, *4*, 7520.

- [29] M. Zhu, O. Cojocaru-Mirédin, A. M. Mio, J. Keutgen, M. Küpers, Y. Yu, J.-Y. Cho, R. Dronskowski, M. Wuttig, *Adv. Mater.* **2018**, *30*, 1706735.
- [30] K. Shportko, S. Kremers, M. Woda, D. Lencer, J. Robertson, M. Wuttig, *Nat. Mater.* **2008**, *7*, 653.
- [31] Y. Cheng, O. Cojocaru-Mirédin, J. Keutgen, Y. Yu, M. Küpers, M. Schumacher, P. Golub, J.-Y. Raty, R. Dronskowski, M. Wuttig, *Adv. Mater.* **2019**, *31*, 1904316.
- [32] J. Keutgen, **2019**, unpublished.
- [33] J. Ma, O. Delaire, A. F. May, C. E. Carlton, M. A. McGuire, L. H. Vanbebbber, D. L. Abernathy, G. Ehlers, T. Hong, A. Huq, W. Tian, V. M. Keppens, Y. Shao-Horn, B. C. Sales, *Nat. Nanotechnol.* **2013**, *8*, 445.
- [34] M. Samanta, S. Roychowdhury, J. Ghatak, S. Perumal, K. Biswas, *Chem. - Eur. J.* **2017**, *23*, 7438.
- [35] a) G. Tan, L.-D. Zhao, F. Shi, J. W. Doak, S.-H. Lo, H. Sun, C. Wolverton, V. P. Dravid, C. Uher, M. G. Kanatzidis, *J. Am. Chem. Soc.* **2014**, *136*, 7006; b) G. Tan, F. Shi, S. Hao, H. Chi, L.-D. Zhao, C. Uher, C. Wolverton, V. P. Dravid, M. G. Kanatzidis, *J. Am. Chem. Soc.* **2015**, *137*, 5100.
- [36] J. Hwang, H. Kim, M.-K. Han, J. Hong, J.-H. Shim, J.-Y. Tak, Y. S. Lim, Y. Jin, J. Kim, H. Park, D.-K. Lee, J.-H. Bahk, S.-J. Kim, W. Kim, *ACS Nano* **2019**, *13*, 8347.
- [37] P. Hopkins, J. Duda, P. Norris, *J. Heat Transfer* **2011**, *133*, 062401.
- [38] J. He, J. Androulakis, M. G. Kanatzidis, V. P. Dravid, *Nano Lett.* **2012**, *12*, 343.
- [39] H. J. Wu, L.-D. Zhao, F. S. Zheng, D. Wu, Y. L. Pei, X. Tong, M. G. Kanatzidis, J. Q. He, *Nat. Commun.* **2014**, *5*, 4515.
- [40] a) O. Cojocaru-Mirédin, P. Choi, R. Wuerz, D. Raabe, *Appl. Phys. Lett.* **2011**, *98*, 103504; b) P. Soni, M. Raghuvanshi, R. Wuerz, B. Berghoff, J. Knoch, D. Raabe, O. Cojocaru-Mirédin, *Sol. Energy Mater. Sol. Cells* **2019**, *195*, 367.
- [41] M. S. Dresselhaus, G. Chen, M. Y. Tang, R. Yang, H. Lee, D. Wang, Z. Ren, J.-P. Fleurial, P. Gogna, *Adv. Mater.* **2007**, *19*, 1043.
- [42] D. G. Cahill, *Rev. Sci. Instrum.* **1990**, *61*, 802.
- [43] R. E. Sittner, K. S. Siegert, P. Jost, C. Schlockermann, F. R. L. Lange, M. Wuttig, *Phys. Status Solidi A* **2013**, *210*, 147.
- [44] K. Thompson, D. Lawrence, D. J. Larson, J. D. Olson, T. F. Kelly, B. Gorman, *Ultramicroscopy* **2007**, *107*, 131.